

Low-resolution detergent tracing in protein crystals using xenon or krypton to enhance X-ray contrast

Oliver Sauer,^a Michel Roth,^b
Tilman Schirmer,^c Gabriele
Rummel^c and Christoph Kratky^{a*}

^aInstitut für Chemie, Karl-Franzens-Universität,
Heinrichstrasse 28, A-8010 Graz, Austria,

^bInstitut de Biologie Structurale Jean-Pierre Ebel,
41 Avenue des Martyrs, F-38027 Grenoble
CEDEX 1, France, and ^cBiozentrum der
Universität Basel, Klingelbergstrasse 70,
CH-4056 Basel, Switzerland

Correspondence e-mail:
christoph.kratky@uni-graz.at

Received 27 June 2001

Accepted 15 October 2001

Xenon and krypton show different solubilities in polar *versus* apolar solvents. Therefore, these noble gases should accumulate in apolar regions of protein crystals. Specifically, they should accumulate in lipid and detergent solvent regions within crystals of membrane proteins, which can be used as a basis for contrast-variation experiments to distinguish such apolar solvent regions from the aqueous phase by a low-resolution X-ray diffraction experiment. This possibility was explored with the OmpF porin, one of the general diffusion pores of the *Escherichia coli* outer membrane. Trigonal crystals were exposed to elevated pressures of the two noble gases (up to 10^7 Pa) for several minutes and subsequently flash-cooled to liquid-nitrogen temperatures. Both rare gases bind to a number of 'specific' sites, which can be classified as 'typical' noble-gas binding sites. Compared with a representative water-soluble protein, they are however much more abundant in OmpF. In addition, a very large number of weakly populated sites are observed which accumulate in the region of the 'detergent belt' for crystals exposed to xenon. After application of a Fourier-filtering protocol, low-resolution images of the detergent belt can be obtained. The resulting maps are similar to maps obtained from low-resolution neutron diffraction experiments on contrast-matched crystals.

1. Introduction

A typical, albeit insufficient, prerequisite for the crystallization of membrane proteins is their solubilization by treatment with a mild detergent (Ostermeier & Michel, 1997; Zulauf, 1985). Once crystallized, the detergent is usually still present in the crystal, where it is responsible for stabilizing the protein and shielding its hydrophobic surface against the aqueous phase. Knowledge of the distribution of the detergent in such crystals provides insight into how the protein is attached to or interacts with the membrane and how the detergent is involved in the crystallization process (Timmins *et al.*, 1994). Functionally relevant regions of lipids and/or detergents have also been observed in crystals of lipases (Hermoso *et al.*, 1997).

While membrane-protein crystals often diffract to high resolution and show a correspondingly well ordered three-dimensional structure, regions occupied by lipid or detergent are always highly disordered. It is difficult to locate or identify such disordered regions by standard protein X-ray crystallography since their structural information is only contained in (often ignored or neglected) low-order reflections. Moreover, the contrast between lipid/detergent and (equally disordered) aqueous solvent is small. Specific techniques have to be

employed to enhance the contrast between detergent and water in the crystal and to collect low-resolution diffraction data. Such experiments have been the realm of neutron crystallography (Timmins, 1995*a*), which exploits the large difference in scattering-length density between hydrogen and deuterium. With neutrons, contrast variation is possible by varying the H₂O/D₂O ratio of the solvent or by using appropriately deuterium-labelled detergents (Hermoso *et al.*, 1997; Pebay-Peyroula *et al.*, 1995; Penel *et al.*, 1998; Roth *et al.*, 1989, 1991; Timmins *et al.*, 1992, 1994; Timmins, 1995*a,b*; Timmins & Zaccari, 1988; Zulauf *et al.*, 1986). These elegant experiments have yielded spectacular insight into the distribution of lipids and detergents in a variety of systems, but they suffer from the low flux of available neutron sources and from difficulties in obtaining isotopically labelled samples.

Macromolecular X-ray crystallography started to exploit contrast-variation techniques at a very early stage (Bragg & Perutz, 1952). Indeed, it was shown repeatedly that the solvent density in protein crystals can be changed by the addition of organic compounds (such as sucrose or glycerol) or ions (*e.g.* caesium, rubidium, bromide, selenate *etc.*) to the mother liquor (Carter *et al.*, 1990; Fourme *et al.*, 1995; Sigler & Blow, 1964) and that this can be exploited to extract information about the phases. By and large, however, contrast variation has been the realm of neutron crystallography (Ibel & Stuhmann, 1975). Moreover, we are not aware of contrast-variation X-ray crystallography being used to distinguish polar from apolar liquid phases in membrane-protein crystals.

Recently, a technique was developed which makes it possible to introduce relatively high concentrations (several hundred millimolar) of xenon and other noble gases into the mother liquor of a protein crystal, often without affecting the crystal's integrity (Sauer *et al.*, 1997; Soltis *et al.*, 1997). The technique involves the exposure of the protein crystal to pressurized gas and the subsequent rapid flash-freezing to liquid-nitrogen temperature. Its original objective was to obtain isomorphous heavy-atom derivatives to solve the crystallographic phase problem by MIR, SIR or MAD techniques. Since the interaction of xenon with the protein is confined to weak dispersion forces, the high interstitial xenon concentration created by exposure to pressurized gas very often has no adverse effects on the crystal packing.

Xenon is a 'soft' noble gas: the diameter of an Xe atom is about 4.2 Å and its atomic polarizability is $\alpha = 4.01 \times 10^{24} \text{ cm}^3$. These properties are similar to those of a methane molecule, which makes xenon with its 54 electrons an ideal hydrophobic probe for X-ray crystallography (Prangé *et al.*, 1998). In fact, a strong preference of xenon for specific apolar sites has emerged from crystallographic experiments (Prangé *et al.*, 1998) as well as from molecular-dynamics simulations (Kocher *et al.*, 1996; Prevost *et al.*, 1996; Tilton *et al.*, 1986). It is well known that the solubility of xenon depends strongly on the polarity of the solvent, which manifests itself in a large difference between xenon solubility in water and *n*-octane (Kennan & Pollack, 1988; Pollack, 1991). Therefore, one might expect that xenon also dissolves more readily in the lipid or detergent phase surrounding membrane proteins than in the

Table 1

Summary of data sets collected from OmpF.

	Nat2	Xe-005a	Xe-050a	Xe-100a	Kr-050a
Pressure (Pa)	0	5×10^5	5×10^6	1×10^7	5×10^6
Beamline	Home	Home	Home	Home	Trieste
Wavelength (Å)	1.5418	1.5418	1.5418	1.5418	0.88
Resolution (Å)	51–3.61	30.7–3.6	46–3.6	14–2.5	23.3–2.2
Completeness (%)	95	98	99	91	98
Redundancy	4.5	2.1	4.9	4.7	7.1
$I/\sigma(I)$ high	3.1	2.7	2.6	2.0	1.4
$I/\sigma(I)$ low	9.6	3.5	6.9	11.0	13.1
R_{sym} (%)	12.2	13.3	16.4	10.8	6.2
R_{anom} (%)	8.6	10.2	10.3	9.2	2.6
Space group	<i>P321</i>	<i>P321</i>	<i>P321</i>	<i>P321</i>	<i>P321</i>
$a = b$ (Å)	117.31	116.98	116.64	116.84	116.90
c (Å)	52.01	51.45	51.69	51.66	51.35
Final R (%)	22.7	23.0	26.9	31.1	28.8

$$\dagger R_{\text{sym}} = \sum |I - \langle I \rangle| / \langle I \rangle. \quad \ddagger R_{\text{anom}} = \sum (|I^+ - I^-|) / \sum (I^+ + I^-).$$

aqueous phase of the mother liquor. Imaging the location of such disordered hydrophobic detergent phases within crystals of membrane proteins should therefore be possible by introducing an electron-density contrast as a result of exposing the crystal to pressurized xenon. Using bulk-solubility data (Pollack, 1991) and simple approximations (*e.g.* the validity of Henry's law), one can estimate that a xenon pressure of 10^5 Pa introduces a contrast of $\Delta\rho \simeq 5 \times 10^{-3} \text{ e \AA}^{-3}$, which is about 1% of the mean electron density of a protein. While it is unclear whether the solubility increases linearly with the pressure at high pressures (Kennan & Pollack, 1990), it is at least plausible to assume an increase of contrast with increasing pressure well beyond ambient conditions. Although beyond 2×10^6 Pa xenon clathrates are formed in aqueous solutions (De Forcrand, 1925), clathrate formation appears to be impeded by most constituents of mother liquors of protein crystals and poses no practical limitation for flash-freezing experiments up to at least 10^7 Pa (Sauer *et al.*, 1997).

Exploratory experiments for its use as a crystallographic heavy atom (Cohen *et al.*, 2001) as well as a probe for hydrophobic protein regions have also been reported for krypton (Alvarez & Prini, 1992; Prangé *et al.*, 1998; Schiltz *et al.*, 1997). Krypton is more inert and less soluble than xenon and its smaller size allows it to occupy smaller cavities, but it interacts less strongly with the protein owing to its lower polarizability (Schiltz *et al.*, 1997). While its reduced solubility may result in a correspondingly smaller contrast-variation signal, the position of its *K* absorption edge ($\sim 0.84 \text{ \AA}$) invites multiple anomalous dispersion experiments (Cohen *et al.*, 2001). For the same reason, krypton might also be a candidate for the MASC method (Fourme *et al.*, 1995) to phase low-order reflections.

In the present communication, we describe contrast-variation experiments with xenon and krypton on the OmpF porin, one of the general diffusion pores of the *E. coli* outer membrane (Schirmer, 1998). OmpF porin is responsible for the uptake of nutrition and the disposal of metabolic waste products. As shown by X-ray crystallography (Cowan *et al.*, 1992), the monomeric protein consists of 16 antiparallel

β -strands forming a slightly ovoid barrel structure. In the membrane it occurs as a homotrimer. The loops which connect the barrel's β -strands are short and regular towards the periplasm ('smooth end') and long, irregular but tightly packed towards the cell exterior ('rough end'). One long loop ('pore constriction loop') contains a short α -helical segment and extends inside the hollow barrel. This loop is believed to control the fine-tuning of the channel characteristics (Huang & Igo, 1996; Phale *et al.*, 1997; Van Gelder *et al.*, 1997).

At the perimeter of the trimer, a hydrophobic band composed mainly of small aliphatic residues can be discerned (Cowan *et al.*, 1992). This would contact the hydrophobic core of the membrane *in vivo*. In the crystals, this part of the surface is covered by detergent molecules as evidenced by low-resolution neutron diffraction studies on tetragonal (Pebay-Peyroula *et al.*, 1995) and trigonal (Penel *et al.*, 1998) OmpF crystals. These contrast-variation studies also allowed discrimination of the tail and head regions of the amphiphiles. For

the tetragonal crystals, the detergent forms a belt surrounding each trimer and is also involved in crystal contacts between trimers. In trigonal OmpF crystals, trimers are arranged in layers perpendicular to the crystallographic triad, leaving solvent-filled channels running parallel to this axis. Within each layer, the trimeric protein is arranged in a pseudo-hexagonal pattern. The detergent is at the inside of such hexagons of trimers, where it surrounds the major solvent channel in a reverse-micelle like fashion. The height of the detergent belt is about 25 Å in both crystal forms, and two 'aromatic girdles' consisting of phenylalanine and tyrosine residues demarcate the detergent domain. These girdles are a characteristic for β -barrel and α -helical membrane proteins (Pautsch & Schulz, 1998) and probably help to anchor the protein in the lipid bilayer.

2. Experimental

Crystals were grown from a buffer containing 0.05 M Tris-HCl pH 9.8 and 0.6% (w/w) *n*-octyl-2-hydroxyethylsulf-oxide and 0.1% octyl POE as detergent, 0.7 M MgCl₂ and 6% (w/w) PEG 2000, the concentration of which was raised to about 10% by microdialysis (Pauptit *et al.*, 1991).

2.1. Preparation of Xe and Kr derivatives

Xenon and krypton derivatives of OmpF porin crystals were obtained with the locally constructed high-pressure device described previously (Sauer *et al.*, 1997). Crystals of typical volumes between 2×10^{-3} and 2×10^{-2} mm³ were transferred from their mother liquor into a cryosolution [same composition as mother liquor plus 10% PEG 200 and 15% (v/v) glycerol] and mounted within a cryoloop (Teng, 1990). Noble-gas

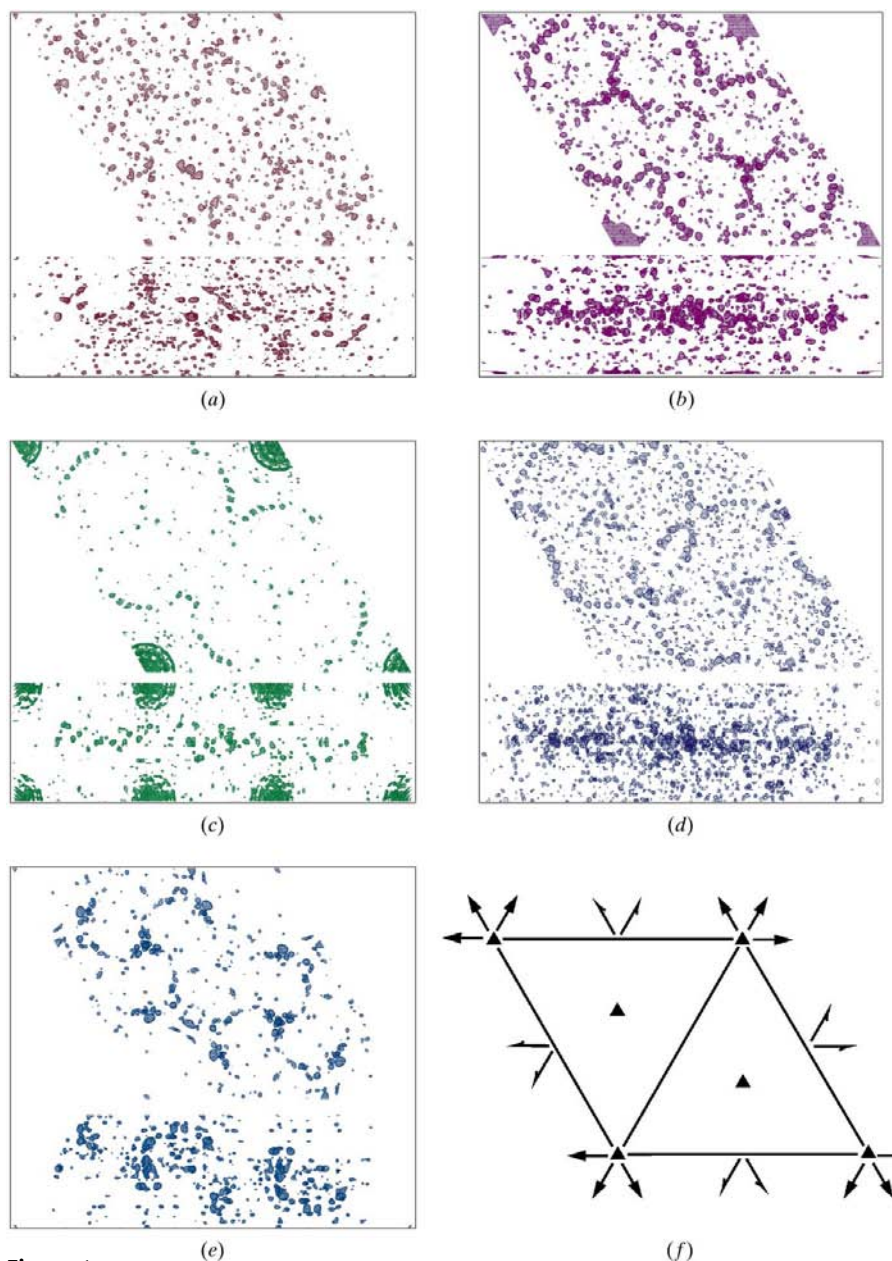


Figure 1

Initial Fourier maps from OmpF after subsection to xenon and krypton. In each of the panels, the density is projected along (upper part of the panel) and perpendicular (lower part of the panel) to the crystallographic threefold axis. (a) Difference density map after exposure to xenon at 5×10^5 Pa, contoured at 3.0σ , (b) 5×10^6 Pa, 2.5σ , (c) 1×10^7 Pa, 3.0σ . (d) Density maps calculated with the observed anomalous differences from OmpF after subsection to 5×10^6 Pa xenon-gas pressure, 2.5σ contours. (e) Difference-density maps after subsection to 5×10^6 Pa krypton gas, 2.8σ contours. (f) The crystallographic symmetry elements of the upper part of each panel.

pressures ranging from 5×10^5 to 1×10^7 Pa (see Table 1) were applied to the crystals for 3–4 min. Immediately after pressure release crystals were flash-frozen (within a few seconds) by dumping into liquid nitrogen.

2.2. Collection of diffraction data

Following flash-freezing, diffraction data were collected either in-house (Siemens rotating-anode generator, Cu $K\alpha$ radiation, mirror collimation system, MAR300 image-plate goniometer) or at the diffraction beamline at Synchrotrone Trieste, Italy.

Care was taken to collect low-resolution data to about 50 Å (see Table 1), using long crystal-to-detector distances (typically 350 mm at our home source) and, where available, a helium path between the crystal and the detector. Crystals diffracted on average to 2.5 Å, but anisotropy reduced the

high-resolution limit in the direction of the c^* axis. This effect increased with gas pressure. A native data set was also collected in-house, using essentially the same data-collection parameters as for the derivatives. Several data sets with different experimental conditions were collected, as summarized in Table 1.

2.3. Data processing

2.3.1. Data reduction. Reflection intensities were integrated with the program *DENZO* (Otwinowski, 1990). The post-refinement was performed with *SCALEPACK* and refined values therefrom were used to reintegrate the images, which were then scaled using *SCALA*, applying local scaling (Collaborative Computational Project, Number 4, 1994). No *B*-factor refinement was applied, because radiation damage

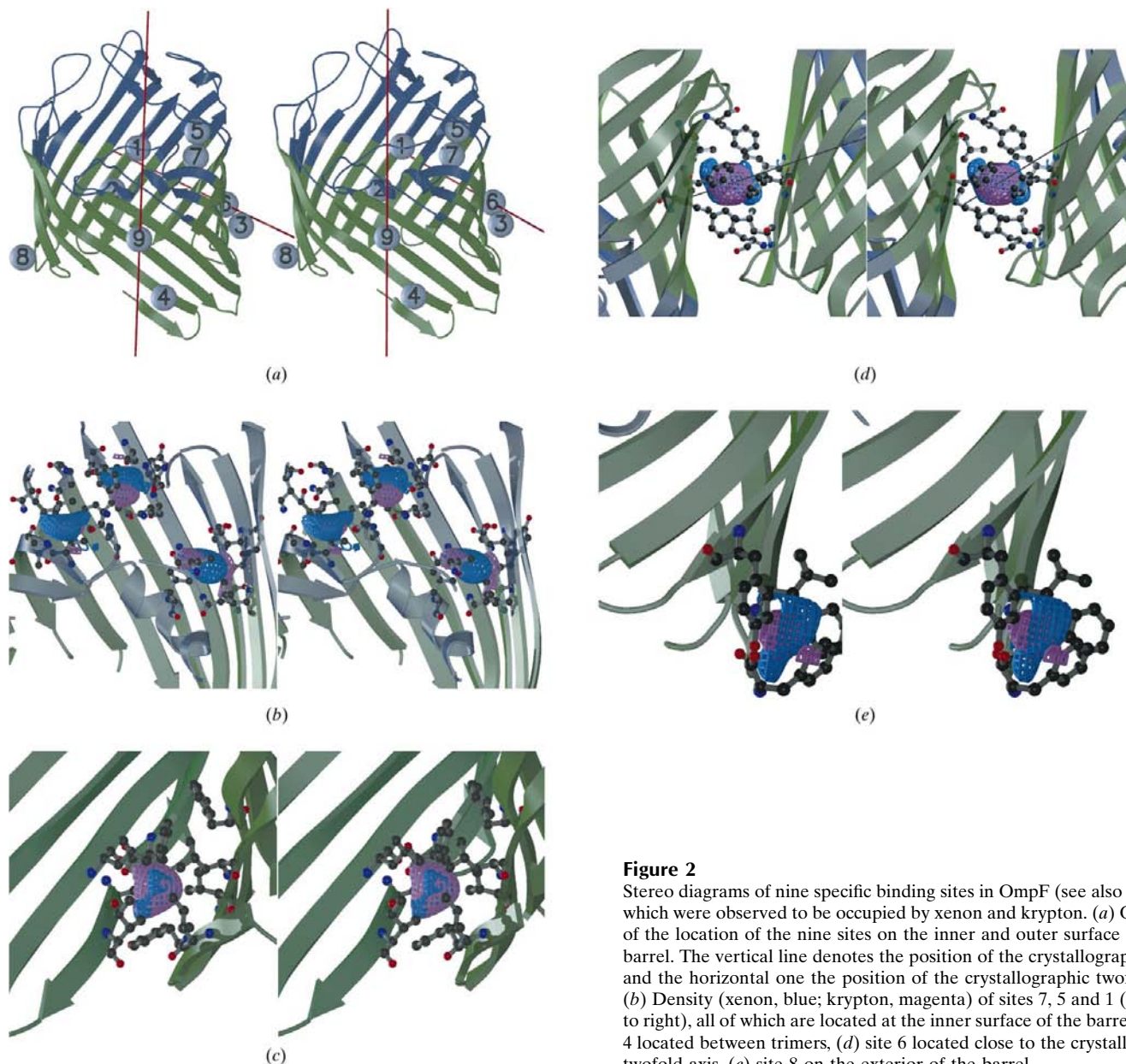


Figure 2
Stereo diagrams of nine specific binding sites in OmpF (see also Table 2), which were observed to be occupied by xenon and krypton. (a) Overview of the location of the nine sites on the inner and outer surface of the β -barrel. The vertical line denotes the position of the crystallographic triad and the horizontal one the position of the crystallographic twofold axis. (b) Density (xenon, blue; krypton, magenta) of sites 7, 5 and 1 (from left to right), all of which are located at the inner surface of the barrel, (c) site 4 located between trimers, (d) site 6 located close to the crystallographic twofold axis, (e) site 8 on the exterior of the barrel.

Table 2

Summary of specific sites occupied by xenon and krypton in OmpF.

Site No.	1	2	3	4	5	6	7	8	9
<i>x, y, z</i> coordinates (Å)	1.9, 34.9, 37.5	−2.4, 32.6, 8.4	20.9, 47.0, 26.2	5.1, 67.4, 18.4	12.4, 40.8, 43.3	19.0, 32.9, 25.9	11.7, 49.1, 40.3	−19.8, 42.3, 18.2	0.0, 67.5, 29.9
Surrounding residues	T122, L258, A215, D256, L109, N230, G232, Y231	A228, L227, A229, L218, K219, Y111, T112, V260	S95, F96, T138, Y139, R140	I3, Y4, A1, V11, L13	F128, F129, G192, A193, A194, A211, E212, Q213	F144, L151, F153, I178, F'144, L'15, F'153, I'178	F128, V133, D134, V136, L158, A170	F265, F267, G268, L269, Y301	L43, W61, F65, L'43, W'6, 1F'65, L''43, W''61, F''65
Hydropathy	−1.1	1.0	−0.1	2.5	0.1	3.6	1.6	1.9	3.8

was found to be negligible and data were collected only to relatively low resolution.

2.3.2. Difference maps, phasing. Phasing was based on the native crystal structure of OmpF porin (Cowan *et al.*, 1992). A protein model devoid of detergent and water molecules was refined against each data set using a rigid-body and subsequently a positional refinement procedure as implemented in program *X-PLOR* (Brünger, 1992). The resulting protein model was very similar to the native OmpF crystal structure for all xenon pressures (r.m.s.d. < 1 Å). No refinement of individual *B* factors was attempted in view of the low resolution. Phases for subsequent difference maps were calculated from the refinement of the protein part of the structure against the native data.

Difference maps using the above phases were calculated for the overlapping resolution range between native and derivative data sets. For the calculation of phases from the native data set, a bulk-solvent correction was applied which was smoothed with a Gaussian ($B = 125 \text{ \AA}^2$) to prevent artefacts near the protein envelope.

2.3.3. Model building. Pseudo-sites were distributed within the difference-density map using the program *MAPMAN* (Kleywegt & Jones, 1996). The threshold limit for the distribution of sites was chosen close to the noise level. Thus, multiple sites may have been assigned to regions of high difference density, but the low threshold value assures that regions of weak density were also accounted for (Kleywegt & Read, 1997; Kleywegt & Jones, 1996). The σ value of each pseudo-site was then plotted against the hydropathy value of the corresponding site. To assign a hydropathy value to a location, the following formula was used:

$$\langle \text{hp} \rangle = \frac{\sum_{i=1}^{\text{alldist}} \text{hp}_i \cdot d_i^{-2}}{\sum_{i=1}^{\text{alldist}} d_i^{-2}}$$

$\langle \text{hp} \rangle$ is the mean hydropathy for the site and d_i is the distance to the closest atom of residue i with hydropathy hp_i (Gilbert, 1992; Kellogg & Abraham, 1992). Hydropathy values were used as implemented in the program *O* (Jones *et al.*, 1991). The corresponding plot of σ versus hydropathy is shown in Fig. 5 for the pseudo-sites obtained from the 5×10^6 Pa Xe experiment (Xe-050a) and was used to determine a σ cutoff level in such a way that the highest peak in the region of negative hydropathy was just below the cutoff. The remaining above-threshold sites were then each populated with a fully

occupied Xe atom with $B = 20 \text{ \AA}^2$ and a structure-factor calculation was performed with these xenon positions. A density map was subsequently computed by Fourier-summation of all $F_c(hkl)$ within a resolution shell between 100 and 10 Å. The resulting map is shown in Fig. 3.

3. Results

We performed a series of experiments with trigonal crystals of the *E. coli* membrane protein OmpF, which were subjected to xenon and krypton gas at elevated pressures and were subsequently flash-frozen by dumping into liquid nitrogen. Pressures of up to 10^7 Pa and exposure times around 3 min were chosen. The frozen crystals were subsequently mounted on a diffractometer under a stream of cold nitrogen (~ 100 K) and X-ray diffraction data were collected. A selection of data sets collected under a variety of experimental conditions is summarized in Table 1. The structures were subsequently solved by molecular replacement, using the protein moiety of the crystal structure of native OmpF as a search model, and refined by rigid-body least-squares methods. Using the phases from this 'protein-only' model, difference-Fourier maps between native and gas-absorbed crystals were calculated. Examples of such initial difference-density maps are shown in Figs. 1(a), 1(b) and 1(c) for xenon, and Fig. 1(e) for krypton. In addition, anomalous maps were computed for Xe-exposed crystals, using the observed anomalous differences as amplitudes of the Fourier summation and the phases obtained from the above 'protein-only' model. Projections of such a map are shown in Fig. 1(d).

Irrespective of the gas pressure, the maps obtained from crystals treated with xenon invariably show numerous patches of difference density which appear to cluster at the envelope around the porin trimers when viewed along the crystallographic triad. When viewed perpendicular to the crystallographic triad, accumulation of density appears roughly in the middle of each protein barrel (Figs. 1a to 1d). Maps obtained from Kr-treated crystals show a somewhat different appearance. Overall, the krypton difference signal is weaker, indicative of the overall lower affinity of krypton. In addition, the signal appears to be confined to fewer sites, which unlike the Xe density do not cluster around the centre of the hydrophobic outer surface of the β -barrels (Fig. 1e).

3.1. Specific binding sites

Positions and heights of most maxima in Fig. 1 depend on the nature of the rare gas (xenon or krypton) and on the experimental conditions (pressure and duration of gas exposure). However, a number of peaks stand out with respect to their height and with respect to the fact that they occur at the same location in xenon and krypton maps under diverse experimental conditions. Table 2 lists nine of these 'specific sites', which were chosen on the basis of their peak height and their consistent occupancy in at least four of the xenon and krypton maps. These sites are located at the outer and at the inner surface of the β -barrel, where cavities appear to have formed by crystal contacts and by the folding of the constriction loop, respectively, as shown in Fig. 2. Site 9 is found on the molecular threefold axis.

3.2. Computation of a low-resolution xenon difference density map

Besides the well populated specific xenon- and krypton-binding sites, the majority of sites observed in the difference density maps (Fig. 1) are only weakly populated and are difficult to interpret in terms of specific interactions between noble-gas atoms and the protein. Moreover, many of these sites are close to the noise level of the map, which makes it difficult to discriminate such weakly populated sites from noise arising from statistical errors, lack of isomorphism or other factors. While the arrangement of non-specific sites appears to be almost random in the case of the krypton maps (Fig. 1*e*), there is a clear pattern in the xenon maps (Figs. 1*a* to 1*d*). Therefore, the remainder of this section will be confined to the processing and analysis of the xenon maps.

In order to make the xenon maps comparable to maps obtained from low-resolution neutron diffraction (Pebay-Peyroula *et al.*, 1995; Penel *et al.*, 1998), a smoothing procedure was applied: possible xenon sites were defined based on peaks in the difference map above a certain threshold (typically between 2.5 and 4.0σ). Xenon atoms ($k = 1.0$, $B = 20 \text{ \AA}^2$) were assigned to the sites and structure factors were calculated from these Xe atoms. Back-transformation yields a (calculated) Xe map at low resolution ($100\text{--}10 \text{ \AA}$). Some of the specific and 'buried' sites located in the interior of the barrel or in regions not accessible to detergent molecules were excluded prior to the computation of the low-resolution map. These sites were Nos. 1, 2, 4, 5, 7 and 9. The resulting map for the 5×10^6 Pa xenon experiment is shown in Fig. 3; a comparison with the corresponding map from neutron contrast-variation studies (Penel *et al.*, 1998) is given in Fig. 4.

3.3. Correlation of xenon sites with polarity

In order to check whether xenon density accumulates preferably at apolar locations, the heights (in σ) of the peaks from the initial difference density map (*e.g.* Fig. 1*b*) were plotted (Fig. 5) against a parameter characterizing the polarity of the corresponding location, *i.e.* the distance-weighted hydrophathy of adjacent protein residues as defined in §2. Evidently, while strong peaks predominantly occur on sites

with positive hydrophathy value (*i.e.* on sites with an apolar environment), weak peaks do not appear to be sensitive to the environment's hydrophathy. In fact, it is probably safe to consider such weak peaks as noise.

4. Discussion

The three-dimensional structure of OmpF (Cowan *et al.*, 1992) consists of a barrel formed by 16 antiparallel β -strands. These barrels occur as homotrimers in the bacterial outer membrane, where they are embedded in such a way that the hydrophobic outer surface of the β -barrels at the perimeter of the trimer matches the core of the membrane. Trimers also occur in trigonal OmpF crystals, where the operation of a crystallographic twofold axis generates a pseudo-hexagonal arrangement of space group $P321$. Crystallization involves the solubilization of OmpF using detergent, which is supposed to replace lipid molecules that interact with the hydrophobic outer surface of the trimer. Owing to their inherent disorder, most of these detergent molecules are invisible in the crystal structure. The objective of the research described in the present communication was to visualize the detergent regions by enhancing their contrast with xenon or krypton.

A number of experiments with different xenon and krypton pressures showed that efficient binding occurs for both rare gases, predominantly in hydrophobic regions of the protein. Both gases occupy a number of specific binding sites, most of them located in cavities within the protein monomer or at the interface between two or three monomers. Many of these 'buried' sites (see Table 2 and Fig. 2) are the same for xenon and krypton. In addition, there are numerous 'open' sites at the surface of the protein where the rare gas is exposed to the surrounding solvent or detergent. It turns out that such 'open' sites are much more efficiently populated by xenon than by krypton.

4.1. Specific 'buried' sites

Nine sites which were found to be consistently occupied both by krypton and by xenon and are completely surrounded by protein residues (from one, two or three monomers) are listed in Table 2 and are shown in Fig. 2. Four of these sites are located inside the β -barrel (sites 1, 2, 5 and 7; Fig. 2*b*) 'above' (*i.e.* towards the extracellular end) the constriction loop. While they are mainly surrounded by hydrophobic residues, there are also a number of hydrophilic residues nearby, which is borne out in a (compared with the other sites) low hydrophathy index (Table 2). The other sites are located on the outside of the barrel. Sites 6 and 9 (Fig. 2*d*) are on crystallographic twofold and threefold symmetry axes, respectively. They are surrounded by exclusively hydrophobic residues. The remaining three sites (3, 4 and 8; Figs. 2*c* and 2*e*) are found within the so-called aromatic belt on the periplasmic side of the barrel and are also predominantly surrounded by aromatic and apolar residues.

These 'cavity' sites observed in OmpF are not untypical for xenon binding. Similar sites, with the xenon surrounded by

apolar residues such as Leu, Val, Ile or Phe, have been observed in many other proteins (Prangé *et al.*, 1998). The hydrophobic sites at the interface between two or three OmpF molecules (sites 4, 6 and 9) correlate with xenon sites occasionally observed between domains or subunits of a protein. An example of such a binding site was recently observed in the crystal structure of glutamate mutase (Reitzer *et al.*, 1999; Sauer, 2001). Compared with other (water-soluble) proteins, OmpF is not outstanding with regard to the nature of the 'buried' binding sites, but rather with regard to their large number.

The observation of specific binding sites for xenon or krypton in OmpF was not the main objective of the present study. For this reason, our diffraction experiments were not optimized to observe such sites, *e.g.* we only collected diffraction data to relatively low resolutions (see Table 1). The data therefore do not permit the refinement of occupancies for these sites, which were only estimated on the basis of the

signal height. However, observation of such sites provides insight into the arrangement of cavities within the protein. Specific binding is required in order to solve the protein structure by isomorphous replacement (MIR) or multiple anomalous dispersion methods (MAD). Typically, the occupancy of these sites is almost independent of the rare-gas pressure. In fact, to observe good occupancy of these 'specific' sites, pressures well below 5×10^6 Pa are sufficient and, at least in the case of xenon, preferable to higher pressures, avoiding the noise of numerous sites of low occupancy. Although the occupancy of these sites appears to be higher for sites with apolar environment, some of the specific sites in OmpF are at least moderately polar. It has been noted previously from xenon derivatives of other proteins that

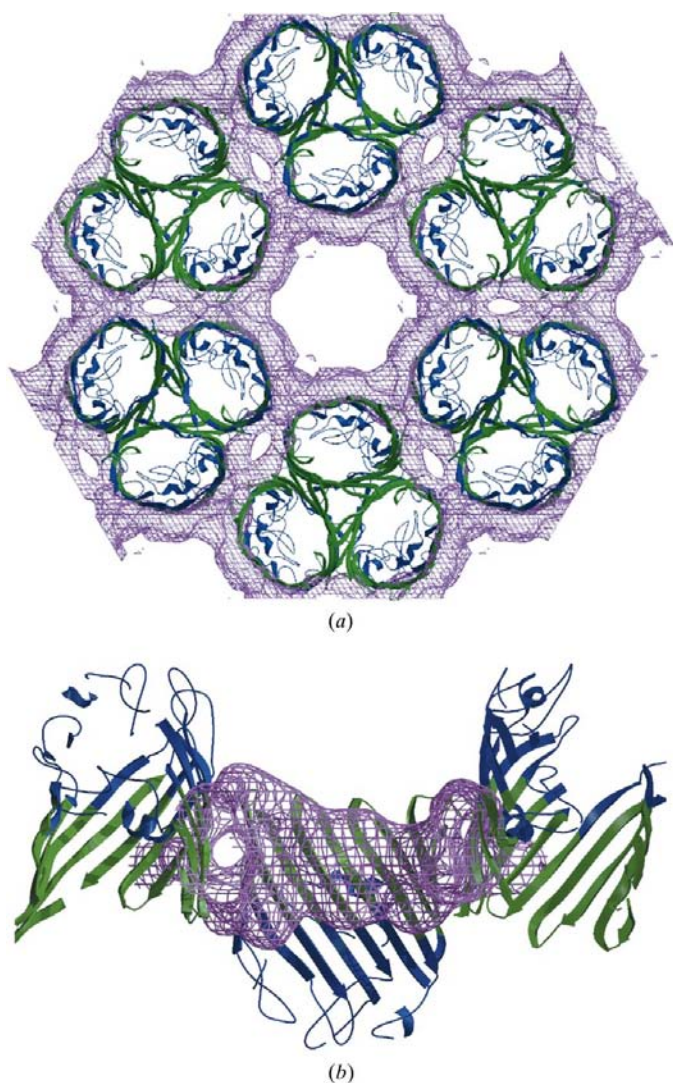


Figure 3
The smoothed low-resolution xenon-enhanced X-ray density map, as obtained from the 5×10^6 Pa experiment. (a) View down and (b) perpendicular to the crystallographic threefold axis.

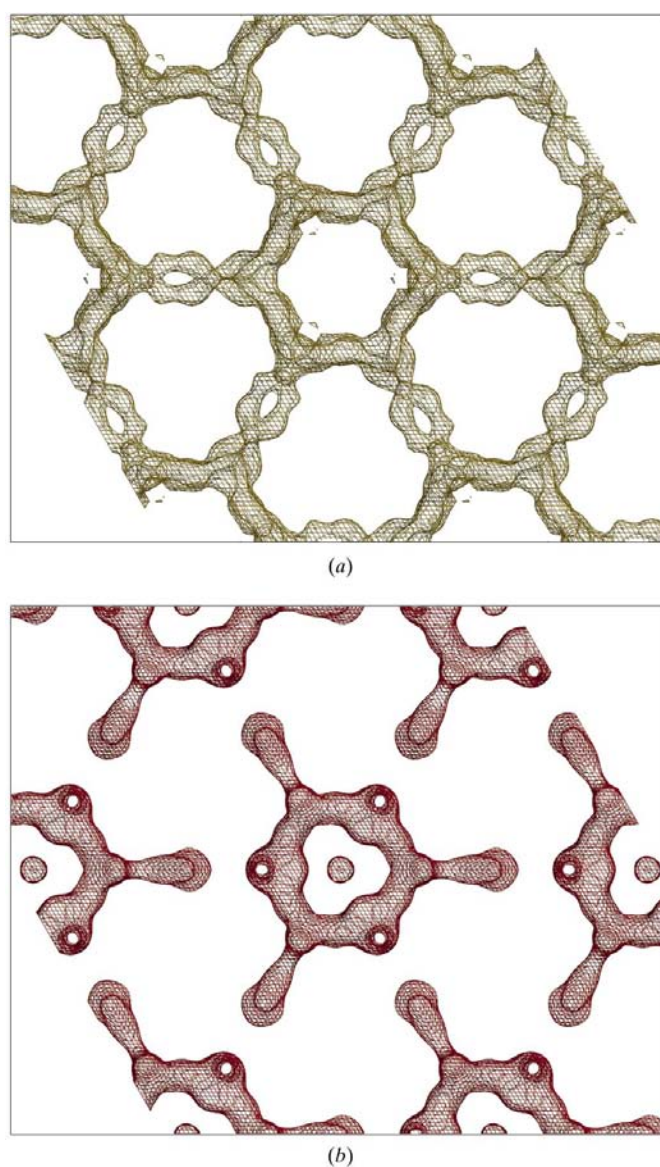


Figure 4
Comparison of low-resolution detergent-tracing maps as obtained by the 5×10^6 Pa xenon-enhanced X-ray (a) and neutron (b) diffraction, projected down the crystallographic threefold axis of trigonal OmpF crystals.

specific binding sites are not confined to a hydrophobic vicinity (Schiltz *et al.*, 1995)

4.2. Xe images detergent regions of OmpF porin

The 'open' sites, which interact with protein side chains pointing into the solvent or detergent region, are much more abundant than the 'buried' sites, but show much lower peak heights owing to partial occupancy. They are populated more efficiently by xenon than by krypton. In order to improve the visibility of their relatively diffuse density, to suppress the inherent noise (originating from experimental errors, lack of isomorphism *etc*) and to obtain a model comparable with the neutron diffraction results, the map was Fourier-filtered as described in §2 and §3. The resulting maps are shown in Fig. 4.

Evidently, the xenon accumulates in a belt surrounding each trimer. The model which we computed from the difference-densities has a belt with an average width around 25 Å. The belt is confined by two rows of aromatic protein residues (mainly Tyr) surrounding the trimer. The thickness of the belt (*i.e.* its maximum distance from the protein surface) is up to 14 Å, which exceeds the length of a C₈ alkyl chain.

There are two types of solvent-filled channels running parallel to the crystallographic *c* axis through trigonal OmpF crystals: larger ones through the origin of the unit cell and smaller ones passing between adjacent trimers. Extensive Xe difference density lines the inner surface of both channels, covering exposed hydrophobic protein surfaces. One can roughly estimate that the volume with increased xenon density in the large channel amounts to approximately 24 000 Å³, which is of the order of 4% of the total cell volume. In the neutron study of trigonal OmpF, the detergent model was found to occupy a much larger volume, as much as 14% of the unit-cell volume including head groups (Penel *et al.*, 1998). Radioactive labelling has indicated a detergent content between 20 and 36% of the cell volume for OmpF crystals (Garavito *et al.*, 1983).

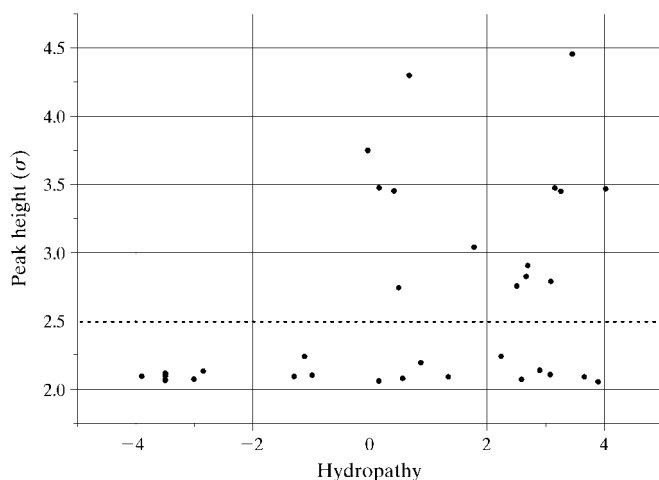


Figure 5
Plot of the peak heights observed in the 5×10^6 Pa xenon difference map (Fig. 1b) versus the hydropathy of the corresponding site. See text for details of the formula used to compute the hydropathy value. The dotted horizontal line indicates the σ -cutoff threshold.

4.3. Neutron versus X-ray imaging

The detergent structure in trigonal OmpF porin crystals was extensively investigated by neutron diffraction (Pebay-Peyroula *et al.*, 1995; Penel *et al.*, 1998). Although the results of this analysis are consistent with the present X-ray study, there are minor discrepancies. Most apparent is the difference in the thickness of the density belt obtained by the two different methods (Fig. 4). Different influences may account for this, but it is difficult to assess their individual contributions.

The most obvious potential cause for discrepancies are differences in the effective crystallographic resolution: while the neutron study was based on data extending to 16 Å, the X-ray data were collected to much higher resolution (3.6 Å or better, see Table 1), but were then Fourier-filtered which effectively reduced the resolution. There are also more subtle methodological differences between the two studies, *e.g.* in the neutron study the detergent region was modelled by regularly distributing pseudo-sites into the experimental neutron density, which were subsequently shifted to minimize the crystallographic residual. In contrast, the X-ray study involved the distribution of Xe atoms on observed but weakly occupied Xe-binding sites. Such sites are predominantly located on the protein surface near hydrophobic residues and it is plausible that many of these sites are located within the interaction area between detergent tails and protein. Further away from the protein surface, Xe atoms probably intercalate between detergent tails, but are likely to be less visible owing to disorder, which rapidly increases with increasing distance from the protein surface (Fig. 6). Consequently, compared with the neutron contrast variation, xenon gives a stronger contrast signal close to the protein surface.

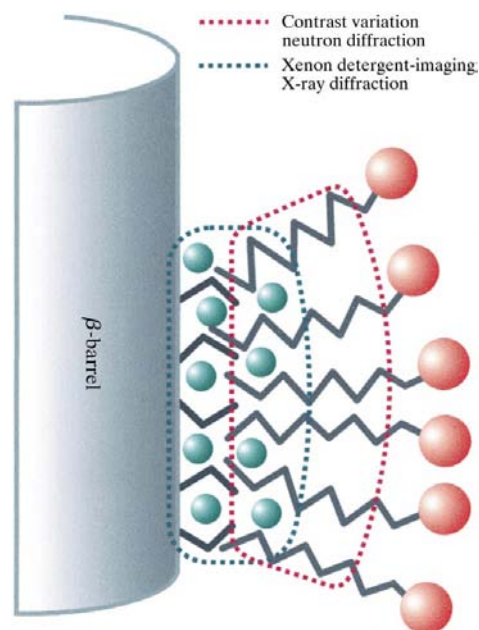


Figure 6
Schematic representation of the reasons for differences in low-resolution detergent-tracing maps as observed by contrast-variation neutron diffraction and by xenon-enhanced X-ray diffraction.

Despite the observation of differently occupied minor sites from one experiment to another, the resulting model after smoothing turns out to be very similar between different experiments. Since the apparent width of the xenon density belt depends somewhat on the resolution employed during back transform, we chose a resolution similar to that of the neutron experiment to obtain comparable results.

4.4. Krypton versus xenon sites

Using similar experimental conditions for producing a xenon and a krypton derivative, the Fourier peak density was found to be smaller in the case of krypton. This is not surprising in view of the fact that Kr is less soluble than Xe and produces an inherently smaller signal owing to its smaller number (by 18) of electrons. The pressure required to attain comparable concentrations of both gases in water was estimated to be about 30% higher for krypton than for xenon (Schiltz *et al.*, 1997).

Nevertheless, it is remarkable that little Kr difference density is found at the interface between detergent and protein, while sites inside the protein or at protein crystal contacts show significant occupancies. The highest Kr peak is located in a cavity confined by Leu109, Thr122 and Leu258 and Asp256 (site No. 1; see Table 2 and Fig. 2*b*). This cavity has a volume of 143 Å³ and emerges when the pore constriction loop folds into the barrel. Xenon also occupies this site, but the highest xenon occupancy occurs at the crystal contact along the twofold axis.

We received financial support from the Österreichischer Fonds zur Förderung der wissenschaftlichen Forschung (Projects Nos. 11599 and 13283) and from the European Commission (TMR project number HPRI-CT-1999-50015). Diffraction data for this project were collected at the following beamlines: EMBL beamline X11 at DESY in Hamburg (Germany), the French CRG beamline D2AM at the ESRF in Grenoble (France) and the diffraction beamline at ELETTRA in Trieste (Italy). We thank the beamline scientists of each facility for their help. The travel expenses for our synchrotron visits were reimbursed by the European Commission through TMR grants allocated to the EMBL outstations in Grenoble and Hamburg and to Sinchrotrone Trieste. We thank Eva Pebay-Peyroula for supplying us with the neutron structure factors of the trigonal OmpF prior to their publication and Raimund Dutzler for his help in obtaining OmpF crystals.

References

Alvarez, J. L. & Prini, R. F. (1992). *J. Chem. Phys.* **96**, 3357–3358.
 Bragg, W. L. & Perutz, M. F. (1952). *Acta Cryst.* **5**, 277–289.
 Brünger, A. T. (1992). *X-PLOR, a System for X-ray Crystallography and NMR*, Version 3.2. New Haven, CT, USA.
 Carter, C. W., Crumley, K. V., Coleman, D. E. & Hage, F. (1990). *Acta Cryst.* **A46**, 57–68.
 Cohen, A. A., Ellis, P. P., Kresge, N. N. & Soltis, S. S. (2001). *Acta Cryst.* **D57**, 233–238.

Collaborative Computational Project, Number 4 (1994). *Acta Cryst.* **D50**, 760–763.
 Cowan, S. W., Schirmer, T., Rummel, G., Steiert, M., Ghosh, R., Pauptit, R. A., Jansonius, J. N. & Rosenbusch, J. P. (1992). *Nature (London)*, **358**, 727–733.
 De Forcrand, M. (1925). *C. Rend. Acad. Sci. Paris*, **181**, 15–17.
 Fourme, R., Shepard, W., Kahn, R., l'Hermite, G. & Li de La Sierra, I. (1995). *J. Synchrotron Rad.* **2**, 36–48.
 Garavito, R. M., Jenkins, J., Jansonius, J. N., Karlsson, R. & Rosenbusch, J. P. (1983). *J. Mol. Biol.* **164**, 313–327.
 Gilbert, R. J. (1992). *J. Mol. Graph.* **10**, 112–119.
 Hermoso, J., Pignol, D., Penel, S., Roth, M., Chapus, C. & Fontecilla-Camps, J. C. (1997). *EMBO J.* **16**, 5531–5536.
 Huang, K. J. & Igo, M. M. (1996). *J. Mol. Biol.* **262**, 615–628.
 Ibel, K. & Stuhmann, H. B. (1975). *J. Mol. Biol.* **93**, 255–265.
 Jones, T. A., Zou, J. Y., Cowan, S. & Kjeldgaard, M. (1991). *Acta Cryst.* **A47**, 110–119.
 Kellogg, G. E. & Abraham, D. J. (1992). *J. Mol. Graph.* **10**, 212–217.
 Kennan, R. P. & Pollack, G. L. (1988). *J. Chem. Phys.* **89**, 517–521.
 Kennan, R. P. & Pollack, G. L. (1990). *J. Chem. Phys.* **93**, 2724–2735.
 Kleywegt, G. J. & Jones, T. A. (1996). *Acta Cryst.* **D52**, 826–828.
 Kleywegt, G. J. & Read, R. J. (1997). *Structure*, **5**, 1557–1569.
 Kocher, J. P., Prevost, M., Wodak, S. J. & Lee, B. (1996). *Structure*, **4**, 1517–1529.
 Ostermeier, C. & Michel, H. (1997). *Curr. Opin. Struct. Biol.* **7**, 697–701.
 Otwinowski, Z. (1990). *DENZO Data Processing Package*. New Haven, CT, USA.
 Pauptit, R. A., Zhang, H., Rummel, G., Schirmer, T., Jansonius, J. N. & Rosenbusch, J. P. (1991). *J. Mol. Biol.* **218**, 505–507.
 Pautsch, A. & Schulz, G. E. (1998). *Nature Struct. Biol.* **5**, 1013–1017.
 Pebay-Peyroula, E., Garavito, R. M., Rosenbusch, J. P., Zulauf, M. & Timmins, P. A. (1995). *Structure*, **3**, 1051–1059.
 Penel, S., Pebay-Peyroula, E., Rosenbusch, J., Rummel, G., Schirmer, T. & Timmins, P. A. (1998). *Biochimie*, **80**, 543–551.
 Phale, P. S., Schirmer, T., Prilipov, A., Lou, K. L., Hardmeyer, A. & Rosenbusch, J. P. (1997). *Proc. Natl Acad. Sci. USA*, **94**, 6741–6745.
 Pollack, G. L. (1991). *Science*, **251**, 1323–1330.
 Prangé, T., Schiltz, M., Pernot, L., Colloch, N., Longhi, S., Bourguet, W. & Fourme, R. (1998). *Proteins Struct. Funct. Genet.* **30**, 61–73.
 Prevost, M., Oliveira, I. T., Kocher, J. P. & Wodak, S. J. (1996). *J. Phys. Chem.* **100**, 2738–2743.
 Reitzer, R., Gruber, K., Jogl, G., Wagner, U. G., Bothe, H., Buckel, W. & Kratky, C. (1999). *Structure*, **7**, 891–902.
 Roth, M., Arnoux, B., Ducruix, A. & Reiss-Nusson, F. (1991). *Biochemistry*, **30**, 9403–9413.
 Roth, M., Lewit-Bentley, A., Michel, H., Deisenhofer, J., Huber, R. & Oesterheld, D. (1989). *Nature (London)*, **340**, 659–662.
 Sauer, O. (2001). *Gases for Structure Determination in Protein Crystallography*. PhD thesis, Karl-Franzens-Universität Graz, Austria.
 Sauer, O., Schmidt, A. & Kratky, C. (1997). *J. Appl. Cryst.* **30**, 476–486.
 Schiltz, M., Fourme, R., Broutin, I. & Prangé, T. (1995). *Structure*, **3**, 309–316.
 Schiltz, M., Shepard, W., Fourme, R., Prangé, T., de La Fortelle, E. & Bricogne, G. (1997). *Acta Cryst.* **D53**, 78–92.
 Schirmer, T. (1998). *J. Struct. Biol.* **121**, 101–109.
 Sigler, P. B. & Blow, D. M. (1964). *J. Mol. Biol.* **14**, 640–644.
 Soltis, S. M., Stowell, M. H. B., Wiener, M. C., Phillips, G. N. & Rees, D. C. (1997). *J. Appl. Cryst.* **30**, 190–194.
 Teng, T. Y. (1990). *J. Appl. Cryst.* **23**, 387–391.
 Tilton, R. F., Case, D. A., Connolly, M. L., Kollman, P. A., Kuntz, I. D., Max, N., Singh, U. C. & Weiner, S. J. (1986). *J. Mol. Biol.* **192**, 443–456.

- Timmins, P. A. (1995a). *Neutron News*, **6**, 13–18.
- Timmins, P. A. (1995b). *Physica B*, **213**, 26–30.
- Timmins, P., Pebay-Peyroula, E. & Welte, W. (1994). *Biophys. Chem.* **53**, 27–36.
- Timmins, P. A., Poliks, B. & Banaszak, L. (1992). *Science*, **257**, 652–655.
- Timmins, P. A. & Zaccai, G. (1988). *Eur. Biophys. J.* **15**, 257–68.
- Van Gelder, P., Saint, N., Phale, P., Eppens, E. F., Prilipov, A., Vanboxtel, R., Rosenbusch, J. P. & Tommassen, J. (1997). *J. Mol. Biol.* **269**, 468–472.
- Zulauf, M. (1985). *Physics of Amphiphiles: Micelles, Vesicles and Microemulsions*, edited by V. Degiorgio & M. Corti, pp. 663–673. Amsterdam: North Holland Press.
- Zulauf, M., Timmins, P. A. & Garavito, R. M. (1986). *Biophys. J.* **53**, 27–36.